JACS
JOURNAL OF THE AMERICAN CHEMICAL SOCIETY
pubs.acs.org/JACS
Article

Microsecond Motion of the Bacterial Transporter EmrE in Lipid Bilayers

Alexander A. Shcherbakov, Merissa Brousseau, Katherine A. Henzler-Wildman, and Mei Hong*

Cite This: https://doi.org/10.1021/jacs.3c00340
Read Online

ABSTRACT: The bacterial transporter EmrE is a homo-dimeric membrane protein that effluxes cationic polyaromatic substrates against the concentration gradient by coupling to proton transport. As the archetype of the small multidrug resistance family of transporters, EmrE structure and dynamics provide atomic insights into the mechanism of transport by this family of proteins. We recently determined high-resolution structures of EmrE in complex with a cationic substrate, tetra(4-fluorophenyl)phosphonium (F_4-TPP^+), using solid-state NMR spectroscopy and an S64V-EmrE mutant. The substrate-bound protein exhibits distinct structures at acidic and basic pH, reflecting changes upon binding or release of a proton from residue E14, respectively. To obtain insight into the protein dynamics that mediate substrate transport, here we measure ^{15}N rotating-frame spin-lattice relaxation ($R_{1\rho}$) rates of F_4-TPP^+-bound S64V-EmrE in lipid bilayers under magic-angle spinning (MAS). Using perdeuterated and back-exchanged protein and ^1H-detected ^{15}N spin-lock experiments under 55 kHz MAS, we measured ^{15}N $R_{1\rho}$ rates site-specifically. Many residues show spin-lock field-dependent ^{15}N $R_{1\rho}$ relaxation rates. This relaxation dispersion indicates the presence of backbone motions at a rate of about 6000 s^{-1} at 280 K for the protein at both acidic and basic pH. This motional rate is 3 orders of magnitude faster than the alternating access rate but is within the range estimated for substrate binding. We propose that these microsecond motions may allow EmrE to sample different conformations to facilitate substrate binding and release from the transport pore.

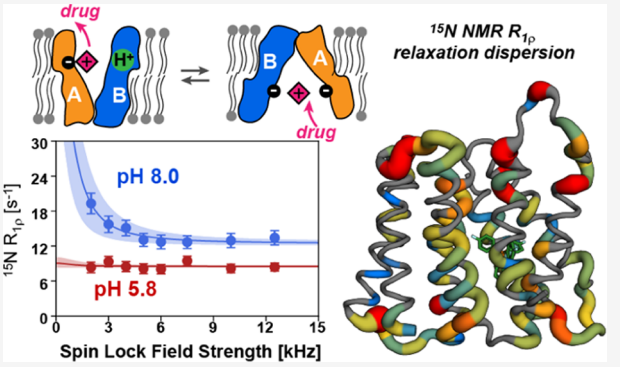

INTRODUCTION

Protein dynamics are crucial for myriad biological processes, including substrate binding and recognition and conformational changes required to bring key functional groups into proximity. To understand the mechanism of action of proteins, an atomic-level description of both the equilibrium ground-state structure and the transient excited-state structures is required.[1−3] In the case of multidrug transporters, dynamics are important for the proteins to interconvert between multiple conformations of the transport cycle. Small multidrug resistance (SMR) transporters efflux quaternary ammonium compounds and other lipophilic cations out of bacterial cells against their concentration gradients to confer resistance to antiseptic and antibiotic compounds.[4] To achieve this, these transporters alternately open to each side of the membrane to move substrates across the lipid bilayer.[5] Importantly, SMR transporters efflux a wide variety of cytotoxic compounds with different shapes, sizes, and chemical properties.[6,7] Thus, these proteins need to change both the sidechain and backbone conformations to accommodate the diverse substrates.[8,9] The conformational plasticity that enables this substrate promiscuity[10,11] has made it difficult to fully characterize the structure and dynamics of these small transporters.

Insights into the structure, dynamics, and mechanism of action of SMR proteins can be gained by studying the archetype member of this family of transporters, EmrE. Found in the inner membrane of the Gram-negative bacteria *Escherichia coli*,[12,13] EmrE is implicated in pH and osmotic stress responses of bacteria, biofilm formation, and resistance to toxic polyaromatic cations.[14−17] Biophysical studies have shown that the transport mechanism of EmrE is complex: The protein can couple the export of toxic substrates to proton import but can also perform substrate-gated proton uniport, and potentially drug uniport or proton-drug symport.[18,19] This mechanistic complexity, together with the substrate promiscuity, implies the existence and dynamic interconversion of many conformational states of the protein. Although structural understanding of EmrE has advanced rapidly in recent years,

Received: January 10, 2023

https://doi.org/10.1021/jacs.3c00340
J. Am. Chem. Soc. XXXX, XXX, XXX−XXX

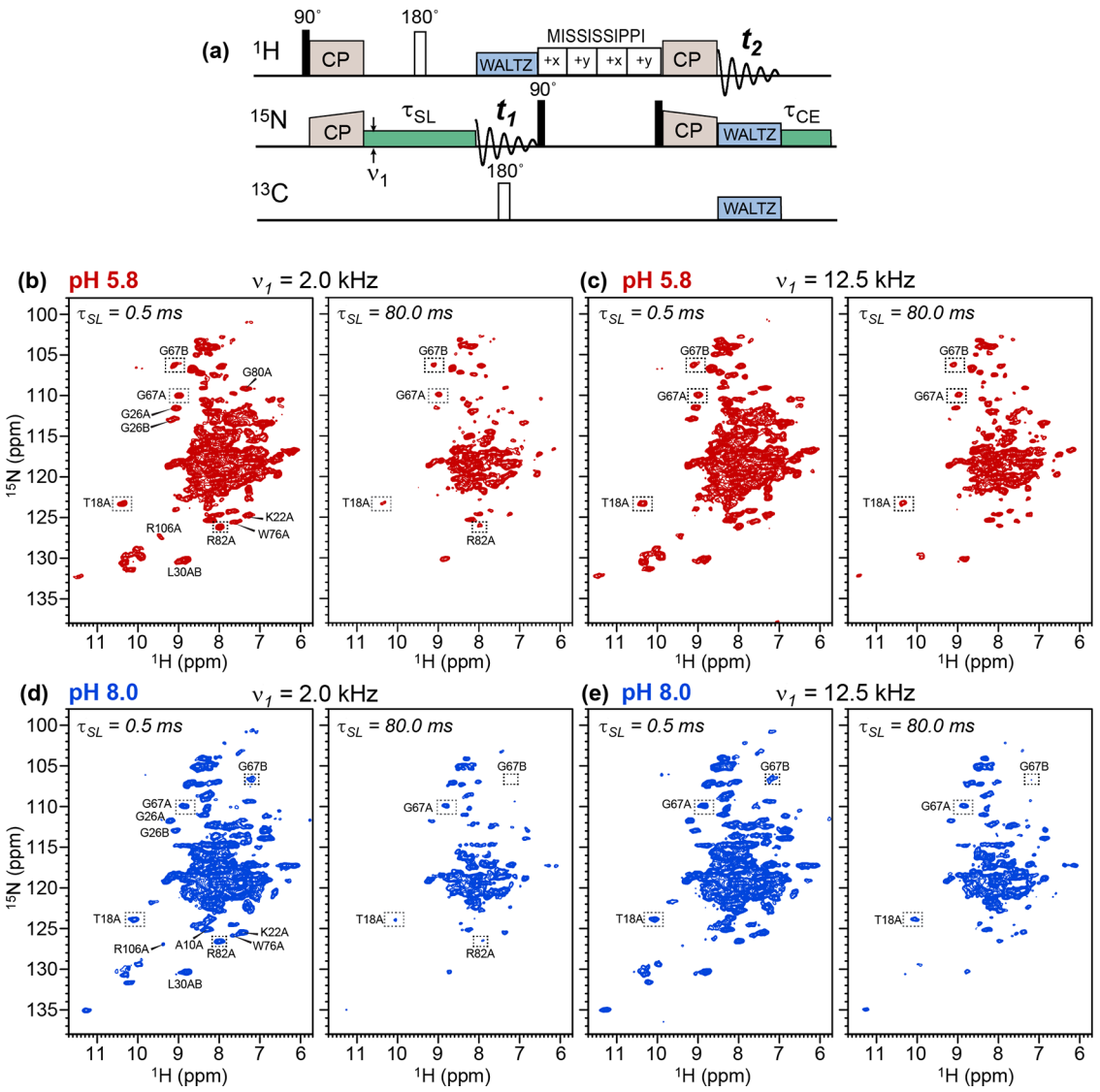

Figure 1. 2D ^{15}N $R_{1\rho}$ relaxation NMR for investigating microsecond motion of membrane-bound EmrE. (a) Pulse sequence diagram of the 2D hNH resolved ^{15}N spin-lock experiment. (b–e) 2D hNH spectra of F_4-TPP$^+$-bound EmrE in DMPC bilayers at different pH under different spin-lock field strengths. (b) Spectra of the pH 5.8 sample measured with ^{15}N τ_{SL} values of 0.5 and 80 ms at a spin-lock field strength of 2 kHz. (c) Spectra of the pH 5.8 sample measured with τ_{SL} values of 0.5 and 80 ms at a spin-lock field strength of 12.5 kHz. (d) Spectra of the pH 8.0 sample measured with ^{15}N τ_{SL} values of 0.5 and 80 ms at a spin-lock field strength of 2 kHz. (e) Spectra of the pH 8.0 sample measured with ^{15}N τ_{SL} values of 0.5 and 80 ms at a spin-lock field strength of 12.5 kHz. Residues in subunits A and B are denoted by letters A and B after the residue number.

the available structures only represent a limited set of functionally relevant states.

Recently, we discovered an S64V mutant of EmrE that possesses the transport activity of the wild-type protein but exhibits slower alternating access,[20] thus providing a good system for high-resolution structure determination. Simultaneously, we developed a high-sensitivity ^{1}H-^{19}F dipolar coupling solid-state NMR technique to measure interatomic distances up to about 2 nm in a high-throughput manner.[21] These two advances allowed us to determine the high-resolution structures of EmrE in lipid bilayers using solid-state NMR. The structures were solved for the protein complexed to a fluorinated analogue of the classical substrate, 4-fluoro-tetraphenylphosphonium (F_4-TPP$^+$). The complex was studied at acidic pH (pH 5.8)[22] and basic pH (pH 8.0),[23] which correspond to the proton-bound and putative periplasm-facing state versus the proton-unbound and putative cytoplasm-facing state, respectively. These structures provided important insights into the structural basis for the weaker substrate affinity at low pH, when EmrE simultaneously binds proton and substrate.

Here, we report site-specific dynamics of F_4-TPP$^+$-bound S64V-EmrE in DMPC bilayers at both low and high pH. We measured ^{15}N $R_{1\rho}$ relaxation rates and their dispersion to determine the rates and amplitudes of protein backbone motions on the microsecond (μs) to millisecond (ms) timescales.[24−28] ^{15}N relaxation dispersion under MAS is similar to $R_{1\rho}$ relaxation in solution, but the former is additionally sensitive to dynamics with rates of tens of kilohertz due to their dependence on the MAS frequency. We conduct high-sensitivity ^{1}H-detected ^{1}H-^{15}N 2D correlation experiments[29−31] under 55 kHz MAS to obtain residue-specific ^{15}N $R_{1\rho}$ relaxation rates of the protein. Our results indicate a global motion with an exchange rate of ~6000 s^{-1}, with varying exchange amplitudes for different TM helices and between different pH. We discuss how these motions may be associated

https://doi.org/10.1021/jacs.3c00340
J. Am. Chem. Soc. XXXX, XXX, XXX−XXX

with substrate binding and release[32] as well as the intrinsic fluctuations of the protein to recognize and accommodate diverse substrates.

MATERIALS AND METHODS

Membrane Protein Samples. The expression, purification, and membrane reconstitution of S64V-EmrE have been described recently.[20,22,23] Samples used in this study were prepared from the recent structure determination studies. Briefly, ^{13}C, ^{2}H, ^{15}N (CDN)-labeled S64V-EmrE was expressed in deuterated media containing 2.5 g/L d_7-^{2}H, ^{13}C-labeled glucose, 1 g/L $^{15}NH_4Cl$ and CDN-labeled ISOGRO. The protein was purified using Ni-NTA affinity column chromatography, followed by thrombin cleavage of the His-tag and size exclusion chromatography. The CDN-labeled EmrE was reconstituted into d_{54}-DMPC (Avanti Polar Lipids) liposomes in protonated buffer by detergent dialysis using 0.5% octyl-glucoside (OG). Thus, all amide hydrogens and other labile hydrogens were back-exchanged to protons. The molar ratio of the protein monomer to DMPC lipids (P: L) was 1: 25. The proteoliposomes were incubated with excess solid F_4-TPP$^+$ at room temperature for at least 16 hours. Excess F_4-TPP$^+$ was then removed by microcentrifugation (20,000*g*, 5 min). Proteoliposomes were pelleted at 100,000*g* and 4 °C for 2 h in an ultracentrifuge, then dried to 40% water by mass in a desiccator. Samples were centrifuged into 1.3 mm MAS rotors. Two samples were used in this study: a pH 5.8 sample containing 0.9 mg S64V-EmrE in a total of ∼3.9 mg proteoliposomes, and a pH 8.0 sample containing 0.9 mg S64V-EmrE in ∼3.6 mg proteoliposomes.

Solid-State NMR Experiments. All ^{15}N $R_{1\rho}$ experiments were conducted on a 600 MHz (14.1 T) Bruker AVANCE III HD spectrometer using a 1.3 mm HCN probe. The samples were spun at 55 kHz, and the sample temperature was maintained at 280 K to match the temperature at which chemical shifts were assigned.[22,23] This sample temperature was reached by setting the bearing gas to 253 K and keeping the water ^{1}H chemical shift δ_{H2O} at 4.94 ppm, based on the empirical relation T_{eff} (K) = 96.9 × (7.83 − δ_{H_2O}).[33] Additional ^{15}N $R_{1\rho}$ data were measured on the low-pH sample at a sample temperature of 305 K, using a bearing gas temperature of 275 K. ^{1}H chemical shifts were internally referenced to match the DSS-referenced solution-state ^{1}H chemical shifts of the protein. ^{15}N chemical shifts were externally referenced to the ^{15}N peak of N-acetylvaline at 122.0 ppm on the liquid ammonia scale.

^{15}N $R_{1\rho}$ relaxation dispersion data of EmrE were measured using a dipolar 2D hNH ^{15}N spin-lock (SL) pulse sequence (Figure 1a). The experiment starts with ^{1}H-^{15}N cross-polarization (CP), followed by a ^{15}N SL pulse of duration τ_{SL}. The relaxation rates were measured for different SL field strengths ν_1. A 180° ^{1}H pulse was applied in the middle of the ^{15}N SL period to suppress ^{1}H-^{15}N J and dipolar coupling. No high-power ^{1}H decoupling was necessary during the spin lock because the sparse ^{1}H network combined with a fast MAS frequency of 55 kHz largely averages the ^{1}H-^{15}N dipolar coupling.[24,28] The ^{15}N SL was followed by ^{15}N chemical shift evolution (t_1) under ^{1}H WALTZ decoupling and ^{13}C *J* decoupling by a 180° ^{13}C pulse. The ^{15}N magnetization was then stored along the z axis for 200 ms, during which water suppression was achieved using the MISSISSIPPI sequence[34] at an rf field strength of 15 kHz. The ^{15}N magnetization was next read out by a 90° pulse and transferred back to ^{1}H by CP for detection under 10 kHz WALTZ decoupling on both the ^{15}N and ^{13}C channels. For the two ^{1}H-^{15}N CP steps, we applied the zero-quantum (ZQ) condition of 0.7ν_r for the ^{15}N rf field (38.5 kHz) and 1.7ν_r for the ^{1}H rf field (93.5 kHz). The ^{15}N rf field strength was ramped 70−100% for ^{1}H-^{15}N forward CP and 100−70% for ^{15}N-^{1}H reverse CP. The CP contact times range from 800 to 1100 μs. For the hard pulses, we used rf field strengths of 83.3 kHz for ^{1}H, 50 kHz for ^{15}N, and 62.5 kHz for ^{13}C.

The rf field strength (ν_1) of the ^{15}N SL pulse was carefully calibrated using nutation experiments. To correct for differential rf heating between experiments with different τ_{SL} values,[35] we applied a constant-energy (CE) compensation pulse with duration τ_{CE} after ^{1}H detection. The sum of τ_{CE} and τ_{SL} is set to 80.1 ms for all of the experiments within each $R_{1\rho}$ decay series.

For the pH 5.8 sample at 280 K, we measured the 2D hNH spectra at eight ^{15}N SL mixing times (0.5, 2.5, 5.0 10.0, 20.0, 40.0, 60.0, and 80.0 ms) for each SL field strength. Eight ^{15}N SL field strengths (2.0, 3.0, 4.0, 5.0, 6.0, 7.5, 10.0, and 12.5 kHz) were used. Therefore, a total of 64 2D spectra were measured. For the pH 8.0 EmrE sample at 280 K, the τ_{SL} values were 0.5, 1.0, 2.5, 5.0, 10.0, 20.0, 40.0, and 80.0 ms and the ^{15}N SL field strengths were 2.0, 2.5, 3.0, 4.0, 5.0, 6.0, 7.5, 10.0, and 12.5 kHz. We also measured the ^{15}N $R_{1\rho}$ of the pH 5.8 sample at a higher temperature of 305 K. For this condition, we chose five mixing times (0.02, 1.0, 3.0, 6.0, 12.0 ms) and four ^{15}N SL field strengths (2.0, 4.0, 8.0, and 12.0 kHz). For all 2D spectra, ^{15}N chemical shift evolution was measured to 45.0 ms using 300 complex t_1 data points. ^{1}H detection was acquired to 25.0 ms using 2500 complex data points. 2D hNH spectra were zero-filled to 4096 complex points in the direct dimension and 1028 complex points in the indirect dimension, then Fourier-transformed and phase-corrected in the TopSpin software. A QSINE apodization with an SSB parameter of 3 was applied to both dimensions.

Extraction of ^{15}N $R_{1\rho}$ Relaxation Times. The ^{15}N $R_{1\rho}$ relaxation modulated 2D hNH spectra were processed using a combination of the Topspin processing function "serial" and Python scripts. Peak intensities were integrated in Topspin by defining an integral region (intreg) file for a reference spectrum, then using the same file for all other 2D spectra using serial processing commands. The integral values were extracted from Bruker's int2D file using a custom Python script along with the ^{15}N chemical shift of each peak for subsequent correction of the measured $R_{1\rho}$ relaxation rates to on-resonance $R_{1\rho}$ values. The integrals of each peak were normalized to the maximum intensity for that residue within a relaxation time series for a specific spin-lock field strength. Uncertainty in the normalized integrals was estimated from the signal-to-noise ratio (SNR) of the peaks and propagated using 2σ errors

$$2 \times \sigma_{I/I_0} = 2 \times \frac{I}{I_0} \times \sqrt{\left(\frac{1}{\mathrm{SNR}_I}\right)^2 + \left(\frac{1}{\mathrm{SNR}_{I_0}}\right)^2} \quad (1)$$

Here, I and I_0 are the integrated intensities of the observed peak and its maximum value in each series, respectively, and SNR_I and SNR_{I0} are the respective signal-to-noise ratios. The observed relaxation decay rates for each peak and each spin-lock field strength were fit to a single-exponential decay function using the SciPy optimization module in Python to extract $R_{1\rho,\mathrm{obs}}$[36]

$$I(t) = A e^{-R_{1\rho,\mathrm{obs}}\, t} \quad (2)$$

We estimated the uncertainties ($\sigma_{R_{1\rho}}$) in the fitted $R_{1\rho}$ parameters using a Monte Carlo analysis as described before.[37] Briefly, 1000 datasets were simulated by multiplying a random number drawn from a standard normal distribution, $p(x) = \frac{1}{\sqrt{2\pi\sigma^2}} e^{-(x-\mu)^2/2\sigma^2}$ with $\mu = 0$ and $\sigma = 0.3$. These parameters were chosen such that nearly all random numbers fall between −1 and 1. This random number was multiplied with the normalized integral error, $2 \times \sigma_{I/I_0}$ (eq 1), and the resulting value was added to the measured intensity I/I_0 to generate the simulated datasets. This procedure randomizes each normalized integral within its 2σ error. These 1000 Monte Carlo datasets were then fit with the same single-exponential decay function using SciPy optimization. The standard deviation of the fit parameters to the Monte Carlo datasets was used as the $\sigma_{R_{1\rho}}$ value, and the $2 \times \sigma_{R_{1\rho}}$ errors were reported.

The experimentally measured $R_{1\rho,\mathrm{obs}}$ values were converted to on-resonance $R_{1\rho}$ rates[37] according to

$$R_{1\rho} = [R_{1\rho,\mathrm{obs}} - \cos^2\theta \cdot R_1]/\sin^2\theta \quad (3)$$

where θ is the angle between the effective ^{15}N spin-lock field and the z-axis. This angle is related to the spin-lock field strength ω_1 and chemical shift offset Ω of each peak by

https://doi.org/10.1021/jacs.3c00340
J. Am. Chem. Soc. XXXX, XXX, XXX−XXX

$$\tan\theta = \omega_1/\Omega \quad (4)$$

In eq 3, a ^{15}N R_1 relaxation rate of ~0.2 s^{-1} was common for solid proteins.[38,39] This R_1 term is a small correction compared to $R_{1\rho,obs}$, which range from 2.3 to 45.9 s^{-1} for 0.5 and 99.5 percentile values for the EmrE samples studied here.

The ^{15}N $R_{1\rho}$ rates as a function of ω_1 were fit to the two-state Bloch−McConnell equation[37,40,41]

$$R_{1\rho}(\omega_1) = R_{1\rho,0} + \phi_{ex}k_{ex}/(\omega_1^2 + k_{ex}^2) \quad (5)$$

Here, $R_{1\rho,0}$ is the rotating-frame spin-lattice relaxation rate in the limit of infinitely strong ω_1 and k_{ex} is the rate constant of exchange. ϕ_{ex} is the exchange amplitude that depends on the populations of the two states, p_A and p_B, and the isotropic chemical shift difference $\Delta\delta$ between them according to $\phi_{ex} = p_A p_B \Delta\delta^2$. Because populations and chemical shift differences are highly correlated, we obtain their product ϕ_{ex} from the fitting. We conducted a global fit of the $R_{1\rho}$ dispersion of all residues using a single k_{ex} value and variable ϕ_{ex} using the LmFit Python package. This was done by setting k_{ex} to be equal for all residues. The k_{ex} was bound to a physically meaningful range of 0 to $(2\pi \times 600)^2$, where the maximum value corresponds to a 10 ppm ^{15}N chemical shift difference on the 14.1 Tesla magnet, and $p_A = p_B$ = 0.5. Fit convergence was tested by attempting 10 global fits with random initial values of $R_{1\rho,0}$, ϕ_{ex}, and k_{ex}. Uncertainties in the Bloch−McConnell fitting were estimated using the same Monte Carlo method as described above using 200 simulated datasets, and 2σ errors were reported. As an alternative approach, we also tested the fitting of the $R_{1\rho}$ dispersion data by allowing different k_{ex} values for different residues.

The ^{15}N $R_{1\rho}$ relaxation data and bar diagrams of $R_{1\rho}$ and ϕ_{ex} values were plotted using the Matplotlib program in Python.[42] Protein structural views of $R_{1\rho}$ and ϕ_{ex} values were generated in PyMol[43] using a Python-PyMol script that uploaded the $R_{1\rho}$ and ϕ_{ex} values as NumPy arrays[44] into the b-factors of the coordinate files. We used the "Putty" representation and the "spectrum b" option for coloring the values. Residues for which no data was available were set to exceedingly small values of 0.1 and were colored gray.

Intrinsic Tryptophan Assays. Purified S64V-EmrE were reconstituted into DMPC/DHPC isotropic bicelles (q = 0.33) as described before. Purified EmrE was reconstituted into liposomes as described above using an EmrE: DMPC molar ratio of 1: 75. Bicelle stock (2×) was prepared separately at pH 5.8 and pH 8.0. Each bicelle stock had 300 mM DMPC in the assay buffer (100 mM MES pH 5.8 or 100 mM Bicine pH 8 and 20 mM NaCl) and was incubated at 45 °C for 1.5 h, then 100 mM DHPC was added, and the solution was incubated for another hour before being subjected to 3 freeze-thaw cycles. F_4-TPP$^+$ was prepared at a maximal concentration of 1 mM in assay buffer with 1× bicelle stock at either pH 5.8 or pH 8.0. 1.3 mM S64V-EmrE in DMPC/DHPC bicelles at pH 7.0 was diluted with 2× bicelle stock and 1× assay buffer to create separate stocks of 40 μM EmrE dimer at pH 5.8 and pH 8.0. 50 μL of this protein solution was mixed with F_4-TPP$^+$ and assay buffer (200 μL total volume) in black 96-well flat-bottom plates and incubated at room temperature for one hour. Samples for pH 5.8 and 8.0 were prepared separately and each F_4-TPP$^+$ concentration was run in triplicate. Endpoint fluorescence was determined using a TECAN Spark with an excitation wavelength of 280 nm (15 nm bandwidth) and an emission wavelength of 340 nm (20 nm bandwidth). The measurement integration time was 40 μs with 50 flashes. The Z-position and gain were determined automatically by the TECAN instrument from the A1 position.

RESULTS

Quantitative studies of EmrE dynamics have so far focused on millisecond-to-second dynamics that are associated with rate-limiting steps in the transport process. To investigate whether the protein undergoes faster internal motions, and whether the protonation states of the two E14 residues affect the protein dynamics on faster timescales, we measured residue-specific ^{15}N rotating-frame spin-lattice relaxation ($R_{1\rho}$) rates of the EmrE-TPP complex. We used CDN-labeled and 100% back-exchanged S64V-EmrE bound to F_4-TPP$^+$ in DMPC bilayers, and conducted ^{1}H-detected 2D hNH correlation experiments with a ^{15}N spin-lock period (Figure 1a). ^{1}H detection dramatically increases the sensitivity of the $R_{1\rho}$ measurements.[45] The experiment was conducted at 280 K to match the temperature at which the ^{1}H and ^{15}N chemical shifts had been measured and assigned.

Under MAS, ^{15}N $R_{1\rho}$ rates depend on the spectral densities $J(\omega)$ at the sum and difference frequencies of the spin-lock field strengths ω_1 and MAS frequency ω_r.[26,28,37,46,47]

$$R_{1\rho,NH} = \frac{1}{20}\left[\frac{\mu_0}{4\pi}\frac{\hbar\gamma_H\gamma_N}{r_{NH}^3}\right]^2\left[\frac{2}{3}(J(\omega_1 + 2\omega_r) + J(\omega_1 - 2\omega_r)) + \frac{4}{3}(J(\omega_1 + \omega_r) + J(\omega_1 - \omega_r)) + 3J(\omega_N) + J(\omega_H - \omega_N) + 6J(\omega_H) + 6J(\omega_H + \omega_N)\right] \quad (6)$$

$$R_{1\rho,N_{CSA}} = \frac{1}{45}(\sigma_\parallel - \sigma_\perp)^2\left[\frac{2}{3}(J(\omega_1 + 2\omega_r) + J(\omega_1 - 2\omega_r)) + \frac{4}{3}(J(\omega_1 + \omega_r) + J(\omega_1 - \omega_r)) + 3J(\omega_N)\right] \quad (7)$$

For $\omega_1/2\pi$ values of 2−12.5 kHz and $\omega_r/2\pi$ of 55 kHz, motions with rates of 55−132 × 10^3 s^{-1} modulate the ^{15}N-^{1}H dipolar coupling and ^{15}N chemical shift anisotropy (CSA) to cause $R_{1\rho}$ relaxation. Therefore, the ^{15}N $R_{1\rho}$ rates measured under our experimental conditions are sensitive to motions on the timescale of 8−18 μs. The effects of microsecond-timescale motion on dipolar- and CSA-driven ^{15}N $R_{1\rho}$ relaxation rates under MAS for perdeuterated and back-exchanged proteins have been numerically simulated and experimentally validated on model proteins.[24,26,28]

Figure 1b−d shows representative 2D hNH spectra of the EmrE-TPP complex at pH 5.8 and pH 8.0, measured using varying ^{15}N spin-lock durations τ_{SL} and spin-lock fields ν_1. Inspection of well-resolved peaks reveals that the relaxation rates are site-specific. For example, the T18A intensity decayed more rapidly than G67A under 2.0 kHz ^{15}N spin-lock (Figure 1b), indicating that T18 in the TM1 helix of subunit A has enhanced dynamics compared to G67 in the TM3 helix. Different residues also exhibit different relaxation dependence on the spin-lock field strength. For example, T18A relaxation is strongly field-dependent, with much slower relaxation under 12.5 kHz spin-lock than under 2.0 kHz spin-lock (Figure 1c). In contrast, G67A relaxation has a weaker field dependence. Thus, T18A is mobile on the 80−500 μs timescale that is probed by the ^{15}N spin-lock (2−12.5 kHz). The fact that the observed relaxation dispersion is residue-specific indicates that it does not result from coherent effects but reflects real differences in the motional rates and amplitudes of the residues. We also detected motional differences between the two subunits. For example, G26 of subunit A has slower relaxation than G26 of subunit B (Figure 1b−e). This difference is present at all of the spin-lock field strengths and at both acidic and basic pH, indicating that the motion is asymmetric between the two subunits. Finally, the high-pH

https://doi.org/10.1021/jacs.3c00340
J. Am. Chem. Soc. XXXX, XXX, XXX−XXX

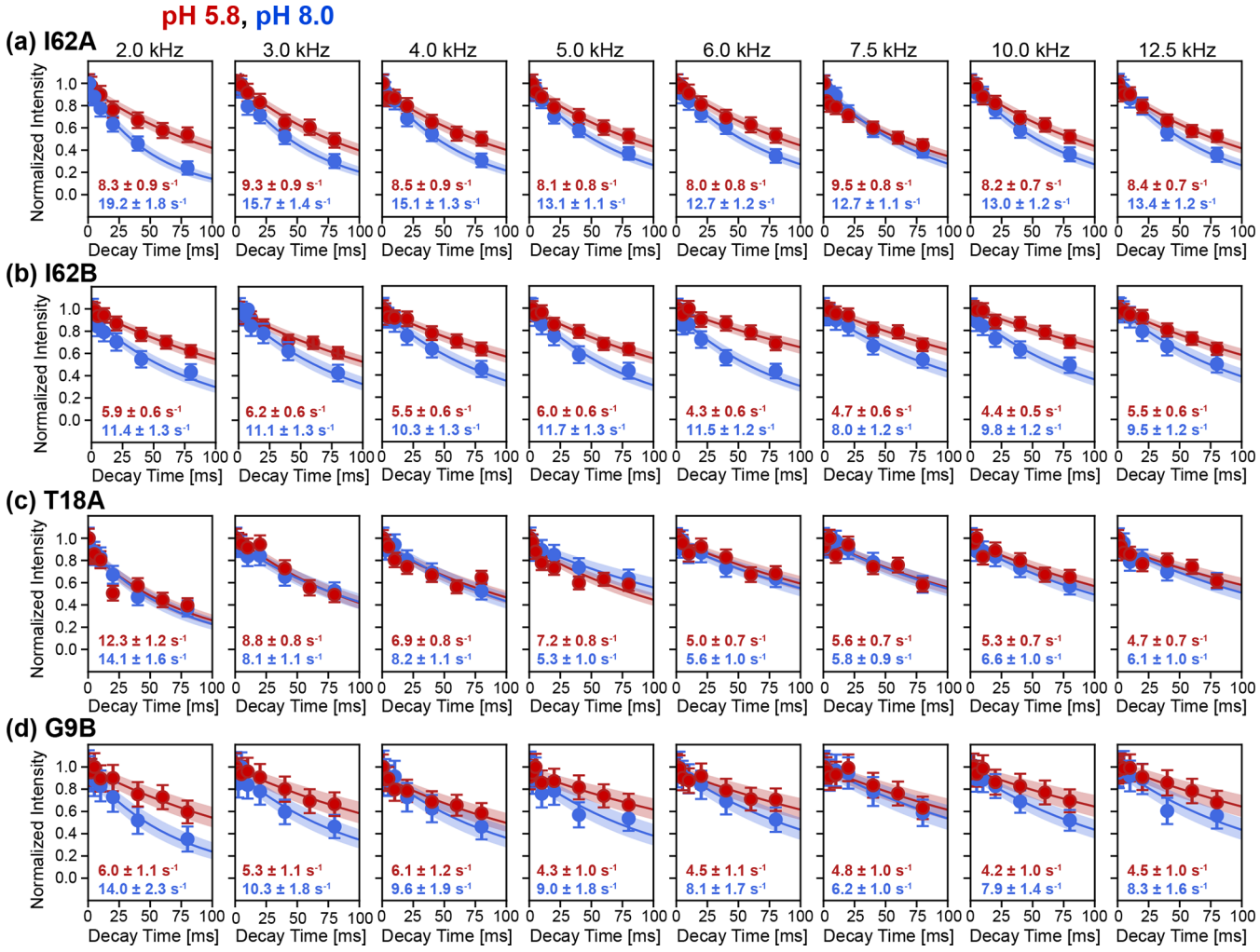

Figure 2. Representative ^{15}N $R_{1\rho}$ decay curves of EmrE at high and low pH at different spin-lock field strengths. In each panel, the pH 5.8 data (red) and pH 8.0 data (blue) are overlaid and compared, and the $R_{1\rho}$ rates are given. Shaded areas represent the 2σ uncertainty around the best-fit curve based on Monte Carlo simulations. (a) I62A in TM3. (b) I62B in TM3. (c) T18A in TM1, one helical turn from the crucial E14 residue. (d) G9B in TM1. Residues in subunits A and B are denoted by letters A and B after the residue number.

spectra show more pronounced intensity decays with τ_{SL} than the low-pH spectra, indicating that the high-pH EmrE-TPP complex is more dynamic. For example, G67B and R82A retain intensities after 80 ms spin-lock in the low-pH complex (Figure 1b,c) but lost the intensities by this time in the high-pH sample (Figure 1d,e).

To obtain the rates and amplitudes of the EmrE motion, we extracted the intensity decays of the cross-peaks at all spin-lock field strengths. These decays fit to single-exponential functions well, giving ^{15}N $R_{1\rho}$ relaxation rates (Figure 2). Many residues such as I62A and G9B (Figure 2a,d) show significant differences in the $R_{1\rho}$ rates between the low-pH and high-pH samples, with the high-pH complex showing faster decays for all sites. Significant relaxation dispersion is observed for some of the residues. For example, at high pH, T18A has a ^{15}N $R_{1\rho}$ of 14.1 s^{-1} under 2.0 kHz spin-lock but only 6.1 s^{-1} under 12.5 kHz spin-lock (Figure 2c). Other residues such as I62A and I62B show little relaxation dispersion (Figure 2a). This confirms that the observed $R_{1\rho}$ dispersion does not result from coherent contributions to ^{15}N relaxation but reflects conformational motions for some of the backbone amides. After correcting for ^{15}N chemical shift offsets, the largest pH dependence of $R_{1\rho}$ relaxation is found in the TM3 helix and in the loop connecting the TM3 and TM4 helices (Figure S1). On average, the high-pH complex exhibits faster relaxation than the low-pH complex. For example, at 2 kHz spin-lock, the average $R_{1\rho}$ value for residues G57A-S75A in TM3 was 10.7 s^{-1} at low pH and increased to 16.3 s^{-1} at high pH. The TM3 helix contains the S64V mutation, which causes a pronounced reduction of the alternating access rate.[20] Thus, motion of the TM3 helix is important for opening and closing the substrate-binding site.

To visualize the site-resolved ^{15}N $R_{1\rho}$ relaxation in the protein, we color-coded the measured ^{15}N $R_{1\rho}$ rates into the antiparallel asymmetric dimer structure of TPP-bound EmrE (Figure 3). For clarity, the two subunits, as defined by their NMR chemical shifts, are shown separately, and the high- and low-pH structures are oppositely oriented to illustrate how the two subunits swap conformations to switch between the open-in and open-out states. It is worth noting that the high- and low-pH structures do not strictly correspond to the putative open-in and open-out conformations in the cell. The cytoplasmic pH is maintained at 7.4−7.6 in *E. coli* while the periplasmic pH is close to the external pH.[48] Laboratory media used for many drug resistance assays is pH 7.4, while *E. coli* is found in a wide variety of pH in the gastrointestinal tract,

https://doi.org/10.1021/jacs.3c00340
J. Am. Chem. Soc. XXXX, XXX, XXX−XXX

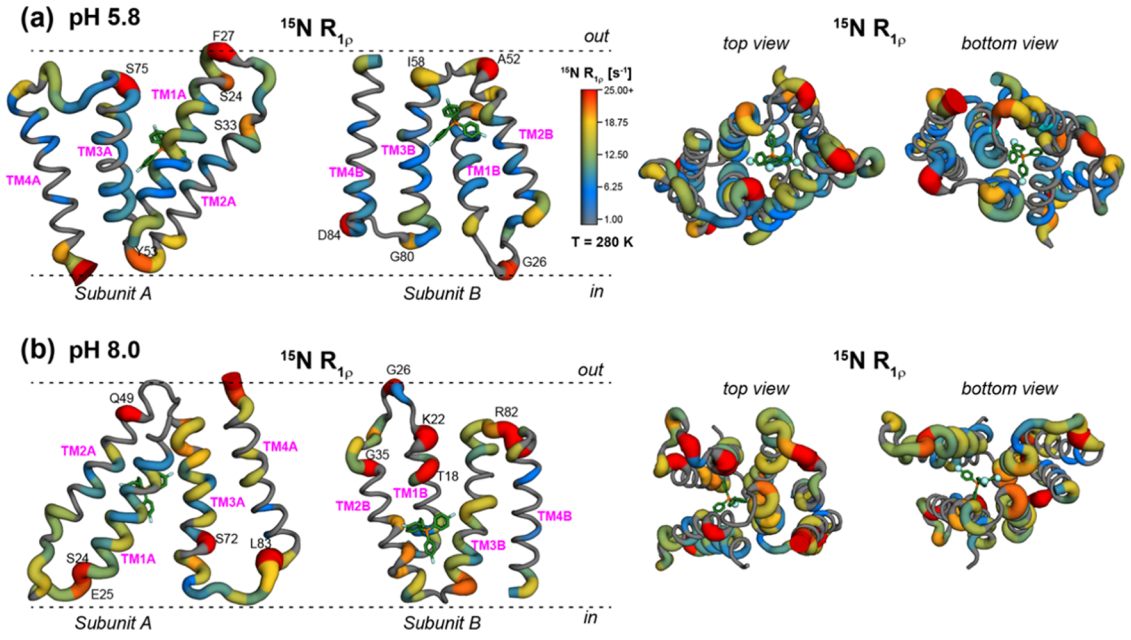

Figure 3. Residue-specific ^{15}N $R_{1\rho}$ rates of F_4-TPP$^+$-bound EmrE at 280 K, color-coded onto the protein structures.[22,23] These $R_{1\rho}$ rates were measured at a spin-lock field strength of 2 kHz. (a) ^{15}N $R_{1\rho}$ rates at pH 5.8. (b) ^{15}N $R_{1\rho}$ rates at pH 8.0. The two structures are shown open to opposite sides of the membrane to illustrate the open-in and open-out conformations. While the *E. coli* cytoplasm is homeostatically maintained near pH 7.4−7.6, the periplasmic pH varies with the external environment and may be lower or higher than the cytoplasmic pH. The fastest-relaxing residues (red) are observed at the loops connecting the TM helices, while the slowest relaxing residues (blue) are observed in the middle of the TM1 and TM3 helices. The high-pH complex exhibits faster $R_{1\rho}$ relaxation than the low-pH complex.

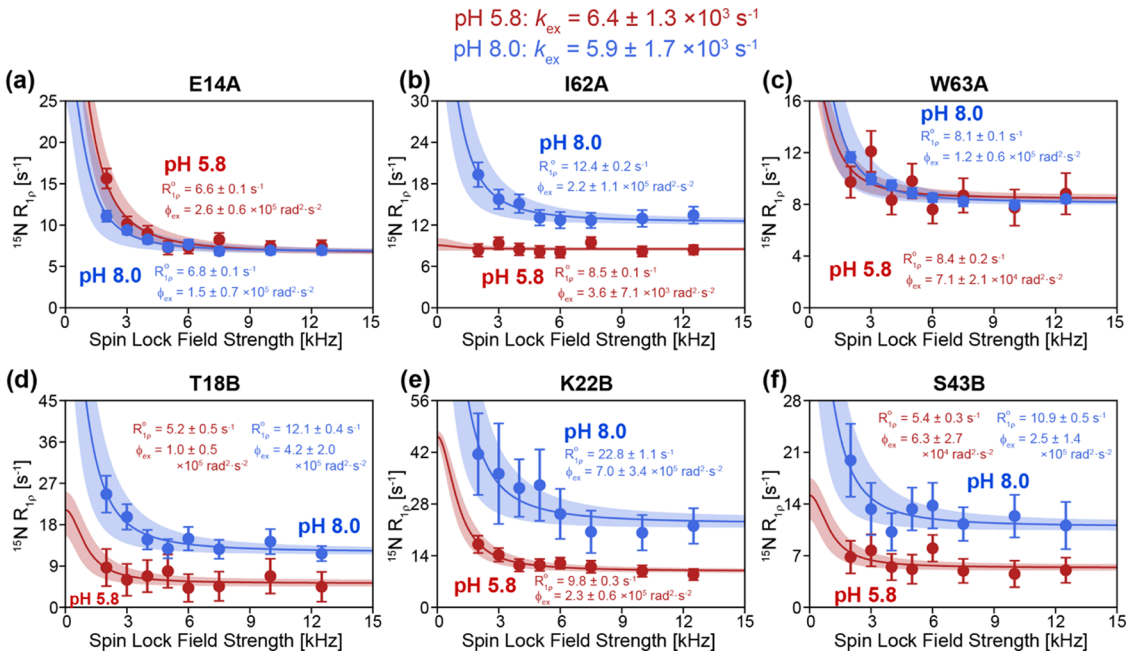

Figure 4. Representative ^{15}N $R_{1\rho}$ relaxation dispersion curves of F_4-TPP$^+$-bound EmrE in DMPC bilayers. The pH 5.8 data are shown in red, while the pH 8.0 data are shown in blue. The extracted $R^0_{1\rho}$ value and ϕ_{ex} value are given in each panel. Residues in subunits A and B are denoted by letters A and B after the residue number. (a) E14A. (b) I62A. (c) W63A. (d) T18B. (e) K22B. (f) S43B. Best-fit ϕ_{ex} and $R^0_{1\rho}$ values were obtained using the two-state Bloch−McConnell model with a global exchange rate k_{ex}. Shaded areas represent the 2σ uncertainty around the best-fit curve based on the Monte Carlo simulations.

urinary tract, intracellular bacterial communities, and other environments. Therefore, whether the cytoplasm is more acidic or more basic than the periplasm depends on the environment. What is clear is that proton binding lowers the affinity of the protein for small-molecule substrates and enhances their off-rate, which is consistent with the more peripheral location of F_4-TPP$^+$ in the low-pH structure. The residue-specific ^{15}N $R_{1\rho}$ rates (Figure 3) indicate that the fastest-relaxing residues are located at the ends of the TM helices and in loops near the lipid−water interface. For example, S24A, F27A, A52B, Y53A, I58B, S75A, G80B, R82B, and L83A exhibit fast relaxation.

https://doi.org/10.1021/jacs.3c00340
J. Am. Chem. Soc. XXXX, XXX, XXX−XXX

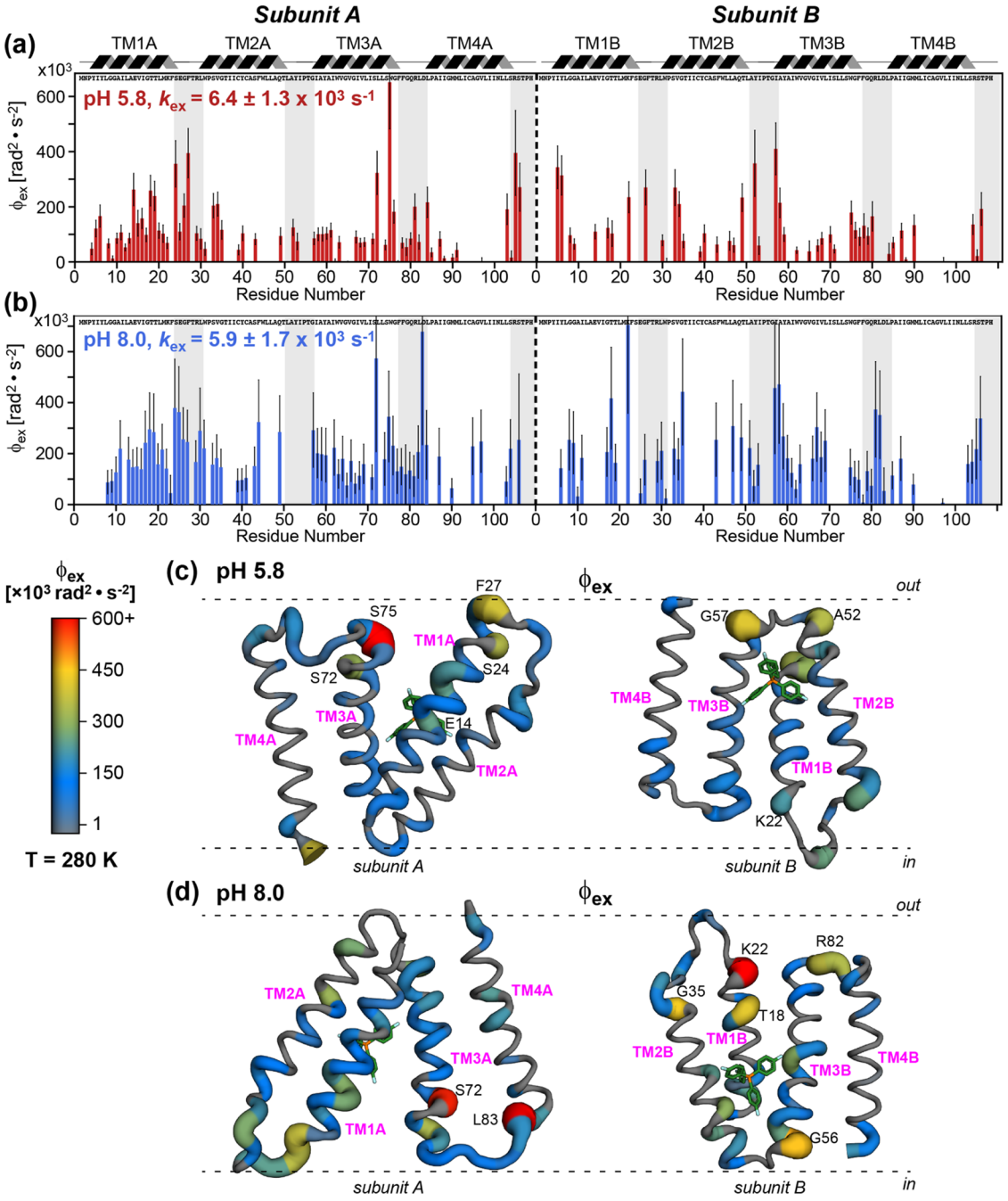

Figure 5. Site-resolved exchange amplitude ϕ_{ex} at 280 K, obtained from best fit of the ^{15}N $R_{1\rho}$ relaxation dispersion curves. (a) pH 5.8 data. (b) pH 8.0 data. The global k_{ex} value of each sample is shown. Gray shaded bars indicate the positions of the interhelical loops. (c) ϕ_{ex} values color-coded onto the pH 5.8 structure. (d) ϕ_{ex} values color-coded onto the pH 8.0 structure. The protein is shown open to either side of the membrane to illustrate the different possible states, although the low- and high-pH structures do not necessarily correspond to the open-out and open-in structures, respectively.

Increasing the pH caused TM3 residues and the C-terminal half of TM1 to exhibit the largest increase in the $R_{1\rho}$ relaxation.

While the ^{15}N $R_{1\rho}$ relaxation is sensitive to 10^5 s^{-1} motions (eqs 6 and 7), the $R_{1\rho}$ relaxation dispersion across spin-lock field strengths of 2 to 12.5 kHz is sensitive to motions with rates of 10^3−10^4 s^{-1}. Using the Bloch-McConell two-state exchange model, we fit the rf field dependence of the $R_{1\rho}$ rates to Lorentzian functions. This fitting allowed the extraction of the product between the populations of the two states and the chemical shift difference between them, as well as the exchange rate k_{ex} (eq 5). Using the offset-corrected relaxation rates, we fit the measured relaxation dispersion using a global k_{ex} for all residues. Representative fits are shown in Figure 4, and the full dataset is shown in Figure S2. The global k_{ex} value is 6.4 ± 1.3 × 10^3 s^{-1} for the low-pH complex and 5.9 ± 1.7 × 10^3 s^{-1} for the high-pH complex. Thus, the global exchange rate is mostly independent of pH. In comparison, different residues show different exchange amplitudes. Residues such as I62A exhibit little dispersion at low pH while residues such as K22B display significant dispersion at high pH. The exchange amplitudes are pH-dependent. For example, I62A displays no relaxation dispersion at low pH but large dispersion at high pH. In

https://doi.org/10.1021/jacs.3c00340
J. Am. Chem. Soc. XXXX, XXX, XXX−XXX

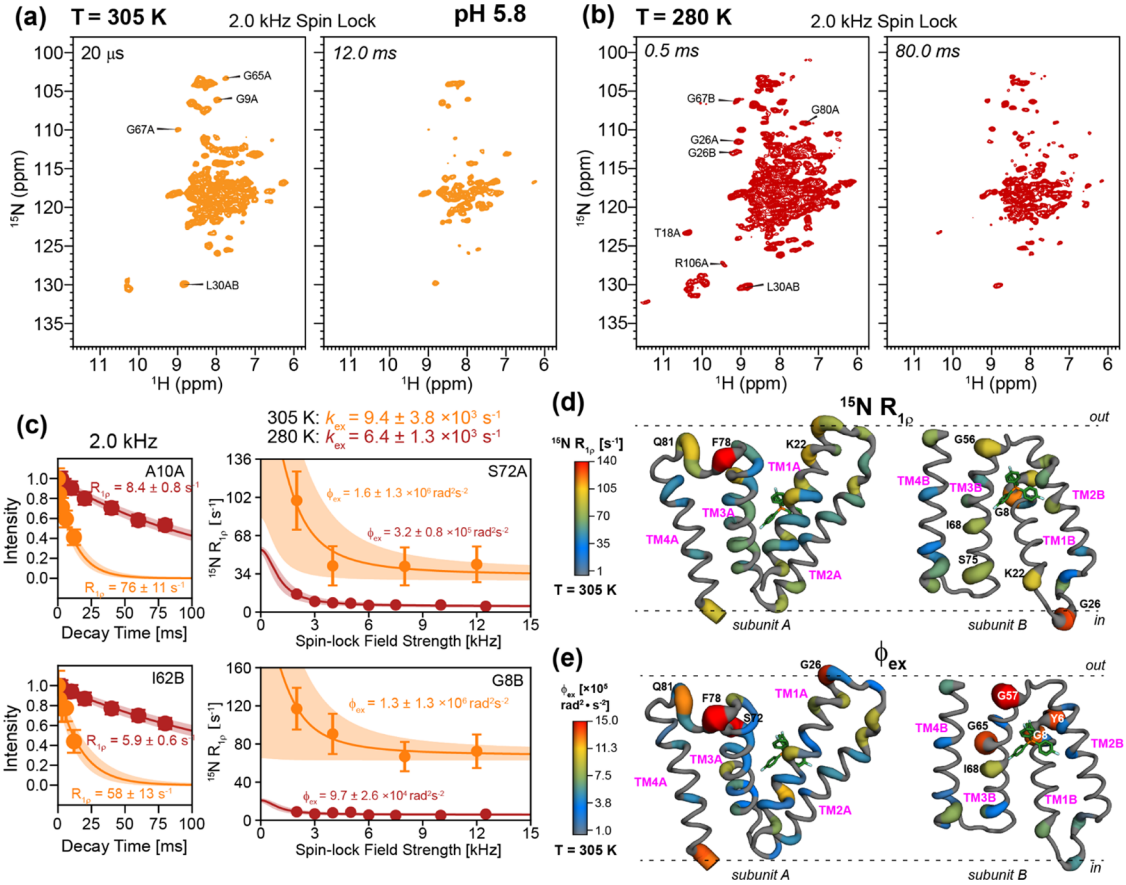

Figure 6. Temperature dependence of the ^{15}N $R_{1\rho}$ relaxation of the low-pH EmrE-TPP complex. (a) 2D hNH spectra measured at 305 K, where the DMPC bilayer is in the liquid-crystalline phase. The spectra were measured with a ^{15}N spin-lock field strength of 2 kHz. (b) 2D hNH spectra measured at 280 K. (c) Left: $R_{1\rho}$ decay curves for representative residues at 305 K (orange) and 280 K (magenta); right: relaxation dispersion curves. Both $R_{1\rho}$ relaxation and relaxation dispersion increase with temperature. (d) 305 K ^{15}N $R_{1\rho}$ rates at 2 kHz spin lock at 305 K, color-coded onto the low-pH structure. Some of the fast-relaxing residues are indicated. (e) 305 K exchange amplitudes ϕ_{ex}, color-coded onto the low-pH structure. The ϕ_{ex} were obtained from best fit of the $R_{1\rho}$ dispersion using a global k_{ex} of 9.4 × 10^3 s^{-1}.

comparison, residues such as E14A show similar $R_{1\rho}$ dispersion at both low and high pH.

The fact that the global exchange rates k_{ex} are similar between the low-pH and high-pH complexes suggests that the outward-facing and inward-facing complexes undergo the same microsecond motion. Indeed, when we attempted to fit k_{ex} residue specifically, we obtained unphysically large variations in both k_{ex} and ϕ_{ex} values for neighboring residues (Figure S3), supporting the view that the microsecond motion observed here is global. To evaluate whether the two subunits of the protein may have different motional rates, we tested fitting the ^{15}N $R_{1\rho}$ dispersion separately for the two subunits, assuming a single k_{ex} value for each subunit. For the pH 5.8 sample, the separate fitting did not yield significantly different k_{ex} values compared to the full-protein fit (Figure S4a,c): monomer A gave a k_{ex} of 6.2 ± 2.4 × 10^3 s^{-1}, whereas monomer B yielded a k_{ex} of 6.6 ± 1.8 × 10^3 s^{-1}. Both values are within the uncertainty of the full-protein k_{ex} of 6.4 ± 1.5 s^{-1}. In comparison, separate-monomer fit of the high-pH data yielded distinct exchange rates of 1.3 ± 0.5 × 10^3 s^{-1} for monomer A and 10.1 ± 1.5 × 10^3 s^{-1} for monomer B, which differ significantly from the full-protein k_{ex} of 5.9 ± 1.8 × 10^3 s^{-1} (Figure S4b,d). However, these separate-monomer fits yielded unphysically large exchange amplitudes for monomer A that would correspond to chemical shift differences of at least 10 ppm. These results suggest that the two monomers do not have significantly different microsecond motions. To obtain additional, more site-specific, dynamics information, measurements such as NERRD dispersion near the MAS frequency would be required.[46,49]

Figure 5 shows site-specific exchange amplitudes for the low-pH and high-pH EmrE-TPP complex based on the global exchange rates. The largest exchange amplitudes are observed in the TM3 helix, with S75A at pH 5.8 and S72A at pH 8.0 exhibiting the highest amplitudes. At high pH, many monomer B residues display large exchange amplitudes. For example, T18, K22, and G35 in the C-terminal half of TM1 to the N-terminal end of TM2 show enhanced ϕ_{ex} values. This region of the protein was previously found to have significant disorder in the high-pH structure.[22,23] In the high-pH complex, residues at the N-terminal end of TM3B and the C-terminal end of TM3A, such as I58B, S72A, and S75A, exhibit large exchange amplitudes, consistent with the fact that these residues are also disordered in the structure.

These ^{15}N $R_{1\rho}$ measurements were carried out below the DMPC phase transition temperature. To investigate if the protein dynamics change significantly in the liquid-crystalline phase, we repeated the ^{15}N $R_{1\rho}$ experiments at 305 K for a smaller number of spin-lock field strengths on the low-pH sample. As expected, the high-temperature spectra have lower sensitivity (Figure 6a) due to the motional averaging of the

https://doi.org/10.1021/jacs.3c00340
J. Am. Chem. Soc. XXXX, XXX, XXX−XXX

^{15}N-^{1}H dipolar couplings. Nevertheless, we resolved many residues in the 2D hNH spectra, which allow us to obtain the $R_{1\rho}$ rates for many residues in the TM1-3 helices. The $R_{1\rho}$ rates are larger at 305 K than at 280 K, as seen by the fact that the remaining intensities in the 12.0 ms spectrum at 305 K (Figure 6a, right) are much lower than the intensities of the 80.0 ms spectrum at 280 K (Figure 6b, right). Intensity analysis showed that $R_{1\rho}$ rates increased by an order of magnitude at the high temperature (Figure 6c, left). The offset-corrected $R_{1\rho}$ rates, mapped onto the structure (Figure 6d), show similar trends as the low-temperature data: the most dynamic segments lie between TM1 and TM2 helices and at the ends of the TM3 helix. We also analyzed the ^{15}N $R_{1\rho}$ dispersion at 305 K. Global fitting using the Bloch-McConnell model yielded an exchange rate of $9.4 \pm 3.8 \times 10^3$ s^{-1} for the low-pH complex, which is 1.5-fold faster than the rate of 6.4×10^3 s^{-1} found at 280 K (Figure 6c). The exchange amplitudes also increased at high temperatures. This is exemplified by S72A, whose ϕ_{ex} value increased from $3.2 \pm 0.8 \times 10^5$ rad^2 s^{-2} at 280 K to $1.6 \pm 1.3 \times 10^6$ rad^2 s^{-2} at 305 K (Figure 6c, right). Interestingly, residues such as G8B, which did not show a significant ϕ_{ex} at 280 K, exhibit a large exchange amplitude at 305 K (Figure 6c). When mapped onto the protein structure, the high-temperature exchange amplitudes (Figure 6e) show similar spatial variation as the low-temperature case, indicating that the same microsecond motions are observed below and above the membrane phase transition.

These ^{15}N $R_{1\rho}$ data indicate that TPP-bound EmrE undergoes a global backbone motion at a rate of ~6000 s^{-1} at both acidic and basic pH. The largest-amplitude motions occur in the C-terminal half of TM1 through the TM1−TM2 loop into the N-terminal portion of TM2 and in the TM3−TM4 loop. Since the water-exposed loop residues may have enhanced hydrogen exchange with the solvent compared to membrane-embedded helices, it is difficult to exclude a contribution of hydrogen exchange to the measured ^{15}N $R_{1\rho}$ rates at the experimental temperature of 280 K. However, the exchange amplitudes vary significantly for different loops and between high and low pH. For example, the TM3−TM4 loop in monomer A has much smaller exchange amplitudes at low pH than at high pH, and this loop also has distinct exchange amplitudes between monomer A and monomer B. These observations imply that hydrogen exchange cannot account for all of the relaxation dispersion, and microsecond motion must be present. Within the helices, the TM3 helix, which contains the S64V mutation and several functionally important ligand-interacting residues such as W63, exhibits larger motional amplitudes than the other helices and is more dynamic at high pH than at low pH. The motional rate k_{ex} increases only moderately from 280 to 305 K, indicating that this dynamics is relatively insensitive to the DMPC phase transition.

DISCUSSION

The ^{15}N $R_{1\rho}$ relaxation rates and dispersion measured here provide new insights into the site-specific motions undertaken by substrate-bound EmrE. The surprising finding is that the S64V mutant, despite its slow alternating access of only 0.6 s^{-1} at 45 °C,[20] undergoes backbone exchange at a rate of about 6000 s^{-1} at 280 K, which increases to 9400 s^{-1} at 305 K. Therefore, EmrE undergoes global microsecond motions that are 3 orders of magnitude faster than the alternating access motion. This microsecond motion occurs with similar rates for the high- and low-pH complexes. Previous measurement of 2D ^{1}H-^{15}N TROSY spectra of apo EmrE in isotropic DMPC/DHPC bicelles found exchange rates of 500 s^{-1} at 45 °C,[10] with an activation energy of 117 kJ mol^{-1}. This data led to the conclusion that EmrE is conformationally plastic, and the fast motion in the absence of ligand is not rate-limiting in the transport cycle. The current data, measured on TPP-bound EmrE, found even faster backbone motions, implying that the conformational plasticity of EmrE is independent of the substrate but is intrinsic to the protein.

We hypothesize that this microsecond motion is intrinsic to the EmrE structure and topology,[50] and may prime the protein for successful binding and recognition of the substrate, and allow the protein to overcome the energy barrier to interconvert between inward- and outward-facing states. Substrate transport across the membrane requires several microscopic steps: substrate binding, protein conformational change that switches binding site accessibility from one side of the membrane to the other, and substrate release. Proton-coupled transport additionally requires coordination of these steps between the transported small molecule and the driving ion, proton. Microscopic rate constants for all of these steps have been estimated for EmrE transport of TPP$^+$ from a combination of NMR and stopped-flow studies[51−53] and have been used to build a kinetic model of transport.[32] Inspection of these estimated rate constants reveals that the on- and off-rates of proton and the small molecule are the only rates in the 10^3−10^4 s^{-1} range, matching the motional timescale probed by the current ^{15}N $R_{1\rho}$ experiments.

The apparent substrate-binding affinity of EmrE is highly dependent on the identity of the substrate[52] and the pH.[19] Stopped-flow data[51] showed that substrate on-rates are diffusion-limited, whereas substrate off-rates vary with the small molecule being released. We used intrinsic tryptophan fluorescence to confirm that the fluorinated substrate, F_4-TPP$^+$, has high affinity for S64V-EmrE (Figure S5). While the protein concentration is constrained to the micromolar regime to maintain bicelle structure and EmrE dimerization, the quenching of intrinsic tryptophan fluorescence occurs at submicromolar concentrations. The affinity cannot be determined quantitatively in this titration regime,[54] but is similar to the affinity of hydrogenated TPP$^+$ to wild-type EmrE, which ranges from a few nanomolar to a few hundred nanomolar depending on pH, temperature, and the membrane-mimetic environment. Given the high affinity, the off-rate is expected to be slow, on the order of 10 s^{-1} as found for TPP$^+$. The reported on-rate for TPP$^+$ is pH-dependent, ranging from 10^5 M^{-1}s^{-1} at low pH to 10^7 M^{-1}s^{-1} at high pH.[51] As a result, the apparent substrate affinity is lower at low pH, requiring higher substrate concentration to saturate binding. While it is difficult to estimate the effective substrate concentration in the solid-state NMR rotor where there is little bulk solvent, substrate concentrations in the range of mM to tens of mM are used to prepare the samples. This would put the F_4-TPP$^+$ on-rate in the range of 10^3 s^{-1}, which is the same timescale as the dynamics observed here. For TPP$^+$-bound wild-type EmrE, the proton off-rate is estimated to be 1600 s^{-1}, and proton release is tightly correlated with the small-molecule on-rate.[51] This similarity suggests that the motion detected by these ^{15}N $R_{1\rho}$ experiments may report on the opening of the transporter loop regions to allow substrate entry.

Even in the substrate-free form, EmrE is dynamic, with rates of 300−500 s^{-1} between 37 and 45 °C.[10] This conformational plasticity is thought to be important for promiscuous

https://doi.org/10.1021/jacs.3c00340
J. Am. Chem. Soc. XXXX, XXX, XXX−XXX

recognition of many substrates by this transporter.[10,11,52] Structurally, this implies that the substrate-binding pocket of the protein must be spacious to permit binding of differently shaped substrates. In turn, this means that the substrate should be dynamic. Indeed, F_4-TPP^+ exhibits motionally averaged ^{19}F NMR spectra.[22,23] Residues known to be important for TPP^+ recognition are clustered in the TM1−TM3 helices, in close proximity to E14. Chemical shift differences between S64V-EmrE bound to TPP^+ or F_4-TPP^+ highlight those residues that directly interact with the substrate and sense the impact of even the small difference in hydrogenation versus fluorination of the substrate.[22] Extensive mutagenesis of EmrE in the past twenty years also implicated additional residues in substrate binding and specificity. These residues are located near the ends of the TM helices and loops, in a pattern similar to the residues that undergo conformational exchange in the $R_{1\rho}$ data. This again suggests that the microsecond dynamics plays a key role in permitting substrate entry and egress.

The pH insensitivity of the exchange rates (k_{ex} values of 5.9−6.4 × 10^3 s^{-1}) obtained from the ^{15}N $R_{1\rho}$ relaxation dispersion data is unexpected since the structures of F_4-TPP^+-bound S64V-EmrE are distinct between low pH and high pH.[22,23] TPP^+ is positioned closer to the open side of the transport pore at low pH[22] but near the middle of the helical bundle at basic pH.[23] The distinct substrate positions suggest that F_4-TPP^+ is primed for exit at acidic pH whenever the loops open sufficiently, whereas substrate entry to the high-pH complex may be limited by the movement of the substrate in the pore to access the deeply embedded E14. The pH insensitivity of the protein dynamics is echoed by the pH insensitivity of the substrate motion. 2D ^{19}F-^{19}F exchange spectra showed that F_4-TPP^+ reorients at similar rates of 137−207 s^{-1} in the high-pH complex and 38−209 s^{-1} in the low-pH complex[23] at 280 K. These data consistently indicate that the internal motions of the EmrE-substrate complex are not strongly controlled by the protonation state of E14, but are intrinsic to the protein. We hypothesize that the structural differences between the low and high-pH complexes and the rapid reorientation of TPP^+ in the binding pocket require a high attempt frequency by the protein to interconvert between the inward-facing and outward-facing states. This high-frequency motion should be pH-independent. Second, although most structural and kinetic studies focus on the role of E14 and the TM helices of EmrE, emerging evidence[18,55,56] implicates that the C-terminal tail may play a role in regulating access to the E14-binding site. It is possible that the microsecond dynamics measured here may partly reflect the pH-independent motion of the C-terminal tail in regulating substrate transport.

The existence of fast protein internal motions to accomplish slower functional processes is common to many membrane proteins. For example, proton conduction by the influenza M2 protein occurs at rates of 10−1000 s^{-1}, but is accompanied by histidine-water proton exchange at rates of 10^5 s^{-1}.[57,58] The rate-limiting step in proton conduction by M2 is the rearrangement of the four-helix bundle between two conformations, which are exclusively controlled by pH.[59,60]

CONCLUSIONS

In summary, the current data demonstrate that ^1H-detected ^{15}N $R_{1\rho}$ relaxation dispersion experiments under fast MAS are an effective approach for obtaining site-specific information about microsecond-timescale motions in membrane transporters. Our data show that substrate-bound EmrE undergoes microsecond motions at both acidic and basic pH. These motions have a global rate of ∼6000 s^{-1} at 280 K at both pH. This rate is 3 orders of magnitude faster than the alternating access rate, and is best attributed to the protein dynamics to allow substrate binding and release. Among the four TM helices, the TM3 helix has the largest motional amplitude, indicating that this helix plays a key role in substrate recognition.

ASSOCIATED CONTENT

Supporting Information

The Supporting Information is available free of charge at https://pubs.acs.org/doi/10.1021/jacs.3c00340.

Additional figures comparing the ^{15}N $R_{1\rho}$ rates at different spin-lock field strengths and pH, full collection of site-specific ^{15}N relaxation dispersion curves, alternative fits of the relaxation dispersion data using residue-specific k_{ex} values and monomer-specific k_{ex} values, tryptophan fluorescence quenching data about F_4-TPP^+ binding to EmrE, and source data of all measured relaxation rates and relaxation dispersion (PDF)

AUTHOR INFORMATION

Corresponding Author

Mei Hong − *Department of Chemistry, Massachusetts Institute of Technology, Cambridge, Massachusetts 02139, United States;* orcid.org/0000-0001-5255-5858; Phone: 617-253-5521; Email: meihong@mit.edu

Authors

Alexander A. Shcherbakov − *Department of Chemistry, Massachusetts Institute of Technology, Cambridge, Massachusetts 02139, United States;* orcid.org/0000-0002-5728-7175

Merissa Brousseau − *Department of Biochemistry, University of Wisconsin at Madison, Madison, Wisconsin 53706, United States;* orcid.org/0000-0003-0555-7177

Katherine A. Henzler-Wildman − *Department of Biochemistry, University of Wisconsin at Madison, Madison, Wisconsin 53706, United States*

Complete contact information is available at: https://pubs.acs.org/10.1021/jacs.3c00340

Notes

The authors declare no competing financial interest.

ACKNOWLEDGMENTS

This work was supported by NIH grants GM088204 to M.H., GM095839 to K.A. H.-W., and the MIT School of Science Camplan Fund to A.A.S. and M.H. The NMR data were measured on NMR spectrometers at the Center for Magnetic Resonance, which is supported by P41 GM132079. Simulations used the NMRbox, which is supported by P41 GM111135.

REFERENCES

(1) Henzler-Wildman, K.; Kern, D. Dynamic personalities of proteins. *Nature* **2007**, *450*, 964−972.

(2) Baldwin, A. J.; Kay, L. E. NMR spectroscopy brings invisible protein states into focus. *Nat. Chem. Biol.* **2009**, *5*, 808−814.

(3) Mandala, V. S.; Williams, J. K.; Hong, M. Structure and Dynamics of Membrane Proteins from Solid-State NMR. *Ann. Rev. Biophys.* **2018**, *47*, 201−222.
(4) Bay, D. C.; Rommens, K. L.; Turner, R. J. Small multidrug resistance proteins: a multidrug transporter family that continues to grow. *Biochim. Biophys. Acta, Biomembr.* **2008**, *1778*, 1814−1838.
(5) Morrison, E. A.; DeKoster, G. T.; Dutta, S.; Vafabakhsh, R.; Clarkson, M. W.; Bahl, A.; et al. Henzler-Wildman, K. A., Antiparallel EmrE exports drugs by exchanging between asymmetric structures. *Nature* **2011**, *481*, 45−50.
(6) Yerushalmi, H.; Lebendiker, M.; Schuldiner, S. EmrE, an Escherichia coli 12-kDa multidrug transporter, exchanges toxic cations and H+ and is soluble in organic solvents. *J. Biol. Chem.* **1995**, *270*, 6856−6863.
(7) Saleh, M.; Bay, D. C.; Turner, R. J. Few conserved amino acids in the small multidrug resistance transporter EmrE influence drug polyselectivity. *Antimicrobial Agents Chemother.* **2018**, *62*, No. e00461-18.
(8) Korkhov, V. M.; Tate, C. G. Electron crystallography reveals plasticity within the drug binding site of the small multidrug transporter EmrE. *J. Mol. Biol.* **2008**, *377*, 1094−1103.
(9) Kermani, A. A.; Macdonald, C. B.; Burata, O. E.; Ben Koff, B.; Koide, A.; Denbaum, E.; et al. Stockbridge, R. B., The structural basis of promiscuity in small multidrug resistance transporters. *Nat. Commun.* **2020**, *11*, No. 6064.
(10) Cho, M.-K.; Gayen, A.; Banigan, J. R.; Leninger, M.; Traaseth, N. J. Intrinsic Conformational Plasticity of Native EmrE Provides a Pathway for Multidrug Resistance. *J. Am. Chem. Soc.* **2014**, *136*, 8072−8080.
(11) Amadi, S. T.; Koteiche, H. A.; Mishra, S.; McHaourab, H. S. Structure, dynamics, and substrate-induced conformational changes of the multidrug transporter EmrE in liposomes. *J. Biol. Chem.* **2010**, *285*, 26710−26718.
(12) Schuldiner, S. EmrE, a model for studying evolution and mechanism of ion-coupled transporters. *Biochim. Biophys. Acta, Proteins Proteomics* **2009**, *1794*, 748−762.
(13) Henzler-Wildman, K. A. Analyzing conformational changes in the transport cycle of EmrE. *Curr. Opin. Struct. Biol.* **2012**, *22*, 38−43.
(14) Sulavik, M. C.; Houseweart, C.; Cramer, C.; Jiwani, N.; Murgolo, N.; Greene, J.; et al. Shimer, G., Antibiotic Susceptibility Profiles of Escherichia coli Strains Lacking Multidrug Efflux Pump Genes. *Antimicrobial Agents Chemother.* **2001**, *45*, 1126−1136.
(15) Nishino, K.; Nikaido, E.; Yamaguchi, A. Regulation and physiological function of multidrug efflux pumps in Escherichia coli and Salmonella. *Biochim. Biophys. Acta, Proteins Proteomics* **2009**, *1794*, 834−843.
(16) Matsumura, K.; Furukawa, S.; Ogihara, H.; Morinaga, Y. Roles of multidrug efflux pumps on the biofilm formation of Escherichia coli K-12. *Biocontrol Sci.* **2011**, *16*, 69−72.
(17) Bay, D. C.; Stremick, C. A.; Slipski, C. J.; Turner, R. J. Secondary multidrug efflux pump mutants alter Escherichia coli biofilm growth in the presence of cationic antimicrobial compounds. *Res. Microbiol.* **2017**, *168*, 208−221.
(18) Spreacker, P. J.; Thomas, N. E.; Beeninga, W. F.; Brousseau, M.; Porter, C. J.; Hibbs, K. M.; Henzler-Wildman, K. A. Activating alternative transport modes in a multidrug resistance efflux pump to confer chemical susceptibility. *Nat. Commun.* **2022**, *13*, No. 7655.
(19) Robinson, A. E.; Thomas, N. E.; Morrison, E. A.; Balthazor, B. M.; Henzler-Wildman, K. A. New free-exchange model of EmrE transport. *Proc. Natl. Acad. Sci. U.S.A.* **2017**, *114*, No. E10083.
(20) Wu, C.; Wynne, S. A.; Thomas, N. E.; Uhlemann, E. M.; Tate, C. G.; Henzler-Wildman, K. A. Identification of an Alternating-Access Dynamics Mutant of EmrE with Impaired Transport. *J. Mol. Biol.* **2019**, *431*, 2777−2789.
(21) Shcherbakov, A. A.; Mandala, V. S.; Hong, M. High-Sensitivity Detection of Nanometer 1H−19F Distances for Protein Structure Determination by 1H-Detected Fast MAS NMR. *J. Phys. Chem. B* **2019**, *123*, 4387−4391.
(22) Shcherbakov, A. A.; Hisao, G.; Mandala, V. S.; Thomas, N. E.; Soltani, M.; Salter, E. A.; et al. Hong, M., Structure and dynamics of the drug-bound bacterial transporter EmrE in lipid bilayers. *Nat. Commun.* **2021**, *12*, No. 172.
(23) Shcherbakov, A. A.; Spreacker, P. J.; Dregni, A. J.; Henzler-Wildman, K. A.; Hong, M. High-pH structure of EmrE reveals the mechanism of proton-coupled substrate transport. *Nat. Commun.* **2022**, *13*, No. 991.
(24) Ma, P.; Haller, J. D.; Zajakala, J.; Macek, P.; Sivertsen, A. C.; Willbold, D.; et al. Schanda, P., Probing transient conformational states of proteins by solid-state R(1ρ) relaxation-dispersion NMR spectroscopy. *Angew. Chem., Int. Ed.* **2014**, *53*, 4312−4317.
(25) Schanda, P.; Ernst, M. Studying dynamics by magic-angle spinning solid-state NMR spectroscopy: Principles and applications to biomolecules. *Prog. Nucl. Magn. Reson. Spectrosc.* **2016**, *96*, 1−46.
(26) Rovó, P.; Linser, R. Microsecond Time Scale Proton Rotating-Frame Relaxation under Magic Angle Spinning. *J. Phys. Chem. B* **2017**, *121*, 6117−6130.
(27) Rovó, P.; Linser, R. Microsecond Timescale Protein Dynamics: a Combined Solid-State NMR Approach. *Chemphyschem* **2018**, *19*, 34−39.
(28) Rovó, P.; Smith, C. A.; Gauto, D.; de Groot, B. L.; Schanda, P.; Linser, R. Mechanistic Insights into Microsecond Time-Scale Motion of Solid Proteins Using Complementary (15)N and (1)H Relaxation Dispersion Techniques. *J. Am. Chem. Soc.* **2019**, *141*, 858−869.
(29) Barbet-Massin, E.; Pell, A. J.; Retel, J. S.; Andreas, L. B.; Jaudzems, K.; Franks, W. T.; et al. Pintacuda, G., Rapid Proton-Detected NMR Assignment for Proteins with Fast Magic Angle Spinning. *J. Am. Chem. Soc.* **2014**, *136*, 12489−12497.
(30) Le Marchand, T.; Schubeis, T.; Bonaccorsi, M.; Paluch, P.; Lalli, D.; Pell, A. J.; et al. Pintacuda, G., (1)H-Detected Biomolecular NMR under Fast Magic-Angle Spinning. *Chem. Rev.* **2022**, *122*, 9943−10018.
(31) Fricke, P.; Chevelkov, V.; Zinke, M.; Giller, K.; Becker, S.; Lange, A. Backbone assignment of perdeuterated proteins by solid-state NMR using proton detection and ultrafast magic-angle spinning. *Nat. Protoc.* **2017**, *12*, 764−782.
(32) Hussey, G. A.; Thomas, N. E.; Henzler-Wildman, K. A. Highly coupled transport can be achieved in free-exchange transport models. *J. Gen. Physiol.* **2020**, *152*, No. e201912437.
(33) Böckmann, A.; Gardiennet, C.; Verel, R.; Hunkeler, A.; Loquet, A.; Pintacuda, G.; et al. Lesage, A., Characterization of different water pools in solid-state NMR protein samples. *J. Biomol. NMR* **2009**, *45*, 319−327.
(34) Zhou, D. H.; Rienstra, C. M. High-performance solvent suppression for proton detected solid-state NMR. *J. Magn. Reson.* **2008**, *192*, 167−172.
(35) Wang, A. C.; Bax, A. Minimizing the effects of radio-frequency heating in multidimensional NMR experiments. *J. Biomol. NMR* **1993**, *3*, 715−720.
(36) Virtanen, P.; Gommers, R.; Oliphant, T. E.; Haberland, M.; Reddy, T.; Cournapeau, D.; et al. SciPy, C., SciPy 1.0: fundamental algorithms for scientific computing in Python. *Nat. Methods* **2020**, *17*, 261−272.
(37) Öster, C.; Kosol, S.; Lewandowski, J. R. Quantifying Microsecond Exchange in Large Protein Complexes with Accelerated Relaxation Dispersion Experiments in the Solid State. *Sci. Rep.* **2019**, *9*, No. 11082.
(38) Öster, C.; Kosol, S.; Hartlmüller, C.; Lamley, J. M.; Iuga, D.; Oss, A.; et al. Lewandowski, J. R., Characterization of Protein−Protein Interfaces in Large Complexes by Solid-State NMR Solvent Paramagnetic Relaxation Enhancements. *J. Am. Chem. Soc.* **2017**, *139*, 12165−12174.
(39) Lamley, J. M.; Öster, C.; Stevens, R. A.; Lewandowski, J. R. Intermolecular Interactions and Protein Dynamics by Solid-State NMR Spectroscopy. *Angew. Chem., Int. Ed.* **2015**, *54*, 15374−15378.
(40) Baldwin, A. J.; Kay, L. E. An R1ρ expression for a spin in chemical exchange between two sites with unequal transverse relaxation rates. *J. Biomol. NMR* **2013**, *55*, 211−218.

https://doi.org/10.1021/jacs.3c00340
J. Am. Chem. Soc. XXXX, XXX, XXX−XXX

(41) Trott, O.; Palmer, A. G., 3rd R1rho relaxation outside of the fast-exchange limit. *J. Magn. Reson.* **2002**, *154*, 157−160.
(42) Hunter, J. D. Matplotlib: A 2D Graphics Environment. *Computing in Science & Engineering* **2007**, *9*, 90−95.
(43) *The PyMOL Molecular Graphics System*, version 1.8; Schrodinger, LLC 2015.
(44) Harris, C. R.; Millman, K. J.; van der Walt, S. J.; Gommers, R.; Virtanen, P.; Cournapeau, D.; et al. Oliphant, T. E., Array programming with NumPy. *Nature* **2020**, *585*, 357−362.
(45) Medeiros-Silva, J.; Mance, D.; Daniëls, M.; Jekhmane, S.; Houben, K.; Baldus, M.; Weingarth, M. 1H-Detected Solid-State NMR Studies of Water-Inaccessible Proteins In Vitro and In Situ. *Angew. Chem., Int. Ed.* **2016**, *55*, 13606−13610.
(46) Marion, D.; Gauto, D. F.; Ayala, I.; Giandoreggio-Barranco, K.; Schanda, P. Microsecond Protein Dynamics from Combined Bloch-McConnell and Near-Rotary-Resonance R(1p) Relaxation-Dispersion MAS NMR. *Chemphyschem* **2019**, *20*, 276−284.
(47) Keeler, E. G.; McDermott, A. E. Rotating Frame Relaxation in Magic Angle Spinning Solid State NMR, a Promising Tool for Characterizing Biopolymer Motion. *Chem. Rev.* **2022**, *122*, 14940−14953.
(48) Bakker, E. P.; Mangerich, W. E. Interconversion of components of the bacterial proton motive force by electrogenic potassium transport. *J. Bacteriol.* **1981**, *147*, 820−826.
(49) Kurauskas, V.; Izmailov, S. A.; Rogacheva, O. N.; Hessel, A.; Ayala, I.; Woodhouse, J.; et al. Schanda, P., Slow conformational exchange and overall rocking motion in ubiquitin protein crystals. *Nat. Commun.* **2017**, *8*, No. 145.
(50) Bahar, I.; Lezon, T. R.; Bakan, A.; Shrivastava, I. H. Normal mode analysis of biomolecular structures: functional mechanisms of membrane proteins. *Chem. Rev.* **2010**, *110*, 1463−1497.
(51) Adam, Y.; Tayer, N.; Rotem, D.; Schreiber, G.; Schuldiner, S. The fast release of sticky protons: kinetics of substrate binding and proton release in a multidrug transporter. *Proc. Natl. Acad. Sci. U.S.A.* **2007**, *104*, 17989−17994.
(52) Morrison, E. A.; Robinson, A. E.; Liu, Y.; Henzler-Wildman, K. A. Asymmetric protonation of EmrE. *J. Gen. Physiol.* **2015**, *146*, 445−461.
(53) Gayen, A.; Leninger, M.; Traaseth, N. J. Protonation of a glutamate residue modulates the dynamics of the drug transporter EmrE. *Nat. Chem. Biol.* **2016**, *12*, 141−145.
(54) Jarmoskaite, I.; AlSadhan, I.; Vaidyanathan, P. P.; Herschlag, D. How to measure and evaluate binding affinities. *eLife* **2020**, *9*, No. e57264.
(55) Glaubitz, C.; Gröger, A.; Gottschalk, K.; Spooner, P.; Watts, A.; Schuldiner, S.; Kessler, H. 31P-CP−MAS NMR studies on TPP+ bound to the ion-coupled multidrug transport protein EmrE. *FEBS Lett.* **2000**, *480*, 127−131.
(56) Thomas, N. E.; Wu, C.; Morrison, E. A.; Robinson, A. E.; Werner, J. P.; Henzler-Wildman, K. A. The C terminus of the bacterial multidrug transporter EmrE couples drug binding to proton release. *J. Biol. Chem.* **2018**, *293*, 19137−19147.
(57) Hu, F.; Luo, W.; Hong, M. Mechanisms of proton conduction and gating by influenza M2 proton channels from solid-state NMR. *Science* **2010**, *330*, 505−508.
(58) Hu, F.; Schmidt-Rohr, K.; Hong, M. NMR detection of pH-dependent histidine-water proton exchange reveals the conduction mechanism of a transmembrane proton channel. *J. Am. Chem. Soc.* **2012**, *134*, 3703−3713.
(59) Mandala, V. S.; Gelenter, M. D.; Hong, M. Transport-Relevant Protein Conformational Dynamics and Water Dynamics on Multiple Time Scales in an Archetypal Proton Channel: Insights from Solid-State NMR. *J. Am. Chem. Soc.* **2018**, *140*, 1514−1524.
(60) Mandala, V. S.; Loftis, A. R.; Shcherbakov, A. A.; Pentelute, B. L.; Hong, M. Atomic structures of closed and open influenza B M2 proton channel reveal the conduction mechanism. *Nat. Struct. Mol. Biol.* **2020**, *27*, 160−167.

https://doi.org/10.1021/jacs.3c00340
J. Am. Chem. Soc. XXXX, XXX, XXX−XXX